Does mixed grain boundary follow the principles of superposition?

Author information

Wei Wan [1, 2], Changxin Tang [2, *] and Eric R. Homer [3]

[1] *Institute for Advanced Study, Nanchang University, Nanchang, 330031, China*

[2] *Institute of Photovoltaics, Nanchang University, Nanchang, 330031, China*

[3] *Department of Mechanical Engineering, Brigham Young University, Provo, 84602, USA*

[*] *Corresponding author, Email address: tcx@ncu.edu.cn*

Abstract

One of the major challenges towards understanding and further utilizing the properties and functional behaviors of grain boundaries (GB) is the complexity of general GBs with mixed tilt and twist character. Here, we demonstrated that the structures and stress fields of mostly mixed GBs could be considered as the superposition of their tilt and twist GB components by computationally examining 26.8 million large-scale structures of 4964 unique silicon mixed GB characters. The results indicate that low angle mixed GB is formed by the dislocation interactions between its decomposed tilt and twist components, while various complex sub-structures with dislocation stress but without conventional dislocation core structures are discovered on twin and structural unit GBs. A universal Read-Shockley model that physically captures the energy trends of the mixed GB is proposed, and its superiority, universality and transferability are proven in a variety of GB structures across different lattices. The validity of this work is confirmed in the comparison with experimental observations and first-principles calculations. Earlier works should now be reassessed in the light of these findings.

Keywords: Grain boundary; Dislocation; Atomistic Simulation; Silicon

1. Introduction

What we know about grain boundaries (GBs) is that they are interfaces separating individual crystals with unique impacts on the structural and functional performances of crystalline materials, such as strength, plasticity, toughness, corrosion resistance and electronic activity [1–6]. Remarkable increments in these performances were made by controlling the population of desired GB types, which was an emerging field called grain boundary engineering (GBE) [7, 8]. Demands of GBE for silicon materials have been raised due to the rapid growth of the semiconductor and photovoltaic industries [9, 10]. Unfortunately, most of our knowledge about GBs was focused on FCC metals with low stacking fault energies [11–15]. To enable the GBE for silicon materials, the structure-property relationships of various silicon GBs are desired. In other words, we need to understand the basic GB structures and energetic properties that determine various GB behaviors (e.g., migration, diffusion, solute segregation and defect sink) [16–26].

Structures and properties of a given GB are jointly defined by the macroscopic and microscopic degrees of freedom (DOFs). The macroscopic DOFs are known as the five GB characters, three of them define the

misorientation axis between two crystals and the other two describe the boundary plane normal. For each unique macroscopic structural descriptor, numerous microscopic DOFs on the GB atomic arrangements have formed a multiplicity of meta-stable structures called GB phases, and their properties play a critical role in the material designs [27–29]. For accurately tracing GB structures at the atomic scale, simulations are usually considered more insightful than experimental methods [30] because some complex GB structures are very difficult for experimental access [31, 32]. Recent trends in this field are relying on the highly transferable artificial neural network interatomic potentials trained by first-principles datasets, which combine the advantages of both electronic structure methods (e.g., first-principles and tight-binding) and semi-empirical interatomic potentials and greatly balance their disadvantages [33–35]. Meanwhile, integrations between GB simulations and the growing machine-learning enable the characterization of almost all GB structures and their properties, which is known as the machine-learning representation of GB structure-property relationships [36–41].

Historically in the studies about GBs in silicon and other materials, the misorientation axis was often simplified down to the misorientation angle, which was based on simple geometry like symmetric tilt or twist [42–45]. Thus, one can define the simplest one-DOF GB on a specific boundary plane normal. The knowledge about the one-DOF GBs and their properties is extensive, including the Read-Shockley relationship [46] that predicts the GB structures and energies as a function of misorientation angle, the Frank-Bilby equation (FBE) [47, 48] predicting dislocation structures of low angle grain boundaries (LAGBs) [49–51], the structural/polyhedral unit models [52–54] characterizing high angle grain boundary (HAGB) structures, the role of disconnection in shaping GB structures [55, 56], the particularity (e.g., high occurrence of frequency, representativeness of entire GB population) of low Σ (reciprocal density) Coincidence Site Lattice (CSL) GBs [12, 57], and the universality of GB structures among different FCC metals [58]. Beyond these findings, the topological analysis of the symmetry of 5D GB space yields a unique strategy named Fundamental Zone, which reveals the role of the boundary plane normal and the misorientation axis [59–62]. The latest computational approach [63] is capable of examining nearly the entire 5D GB space due to the rapid development of computer resources.

Although these reviewed studies almost constructed today's understandings of GB, they still lack comprehensive coverage of the possible GB characters because an arbitrary GB is not limited to the widely studied one-DOF symmetric tilt or twist types. Once geometrically available, the co-existence of symmetric tilt and twist DOFs, known as the mixed tilt-twist GB character, appears. Earlier works [64–66] have suggested an analytical method for studying this GB type through its decomposition into tilt and twist components with the nearest crystallographic distances, and addressing the correlations within. For example, low angle symmetric tilt grain boundaries (LASTGBs) are often considered as dislocation arrays that fall in the prediction of FBE [67, 68], and low angle twist grain boundaries (LATwGBs) are reported as dislocation networks with quadrate, hexagonal or more complex topology [69–73]. Going further, it has been experimentally and numerically shown that the low angle mixed grain boundaries (LAMGBs) contain dislocation characteristics of its two components [66, 74–77]. Meanwhile, further knowledge about the mixed GB character and its structure-property relationships is quite limited [78], and therefore raised some intriguing

questions: 1) What is their common structural feature? 2) How does the property (e.g., energy and mobility) vary with the two DOFs? 3) Most importantly, can we transfer the knowledge about the one-DOF GBs to them?

In this atomistic study, we compute silicon mixed GB structures near the common <100>, <110> and <111> misorientation axes with classical molecular mechanics. The unique protocol of this study is that the mixed GBs are studied by decomposing into the tilt and twist components, which allows us to understand the correlations among tilt, twist and mixed tilt-twist GB geometry. Contrary to previous works that typically address GBs with only one DOF, we analyzed the mixed GBs within a 2D space and established a universal model on the basis of the classical Read-Shockley framework to characterize most of the mixed GB energies.
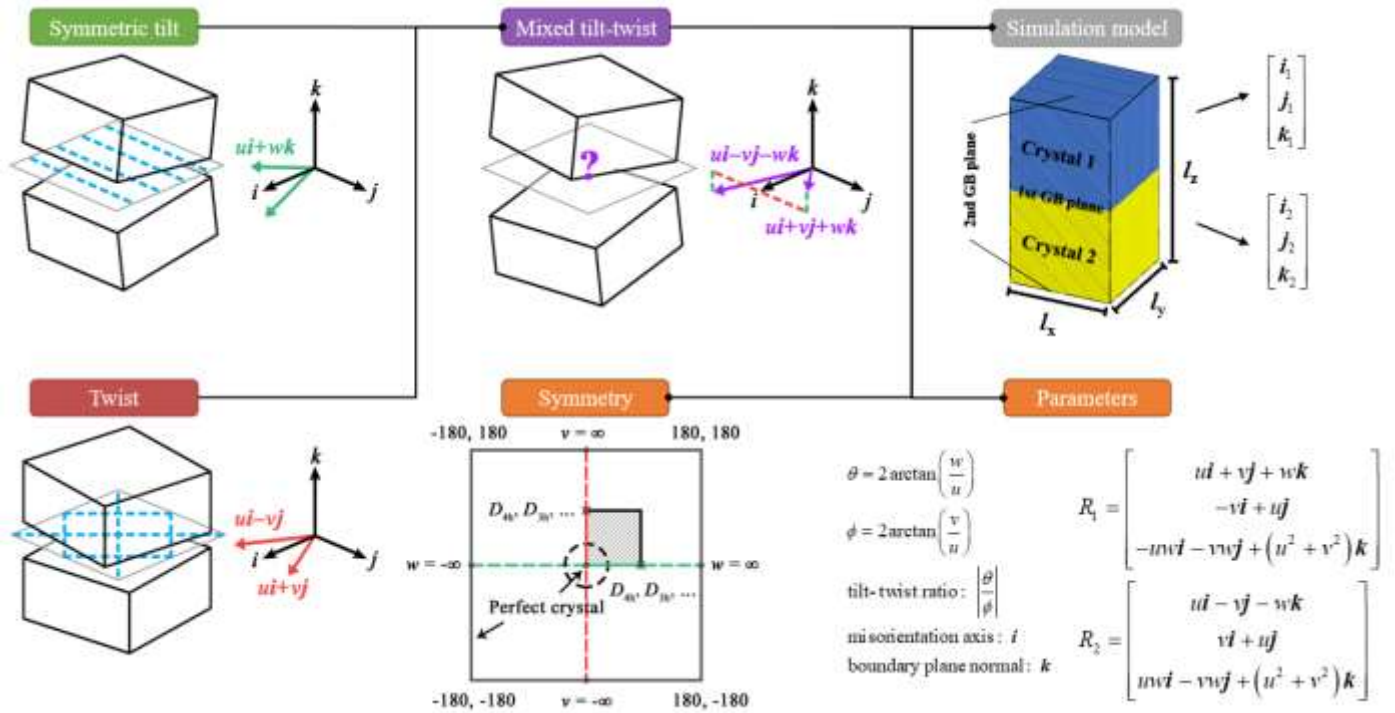
2. Methodology

Figure 1. Geometry settings of the mixed tilt-twist GB character. A given mixed GB is generated in the *ij* plane with misorientation axis *i* and boundary plane normal *k*, and the rotation matrices of the upper crystal 1 and the lower crystal 2 are defined as $R_1 = [i_1\, j_1\, k_1]$ and $R_2 = [i_2\, j_2\, k_2]$. The mixed GB decomposes into a symmetric tilt grain boundary (STGB) with tilt angle θ and a twist grain boundary (TwGB) with twist angle ϕ at *ik* and *ij* planes, respectively. The co-existing tilt and twist angles create a 2D mixed character space with symmetry drawn in Figure 1. The domain of the mixed character space is [-180°, 180°] × [-180°, 180°]. The domain center (0°, 0°) and all four domain boundaries are perfect crystals or asymmetric tilt grain boundaries (ATGB, depending on the selection of *i*). LAMGB are found around the domain center (black dashed circle) and other positions where the perfect crystals appear (depending on the selection of *i* and *k*). STGBs and TwGBs are located in the 1D subsets [-180°, 180°] × [0°] and [0°] × [-180°, 180°], respectively. The symmetry of the axes *i* and *k* determines the perfect crystals and symmetric equivalence in the two mentioned 1D subsets (marked by the × symbol; For example, 90° for D_{4h} symmetry and 180° for D_{2h} symmetry). Noting that the co-existing tilt and twist angles would make boundary plane normal k_1 and k_2 varies, and thus the mixed character space is unable to uniquely index a GB character.

The mixed GB are identified by their boundary plane and misorientation axis. For example, (001)/[100] mixed GB denotes that the boundary plane is (001) while the misorientation axis is [100]. Three combinations of boundary plane and misorientation axis are considered, including (001)/[100], (011)/[100] and (111)/[110]

3

mixed GBs, resulting in three mixed character spaces. 1024 (32 STGBs and 32 TwGBs), 1536 (48 STGBs and 32 TwGBs) and 2304 (48 STGBs and 48 TwGBs) mixed GBs are sampled for (001)/[100], (011)/[100] and (111)/[110] mixed character spaces, respectively, which guarantee a comprehensive coverage at $\sim 3° \times 3°$ resolution. Tables S1-S6 in the Supporting Information show the details of sampled tilt and twist GBs, and Figure 1 shows the geometry of mixed GB. All details of the sampled GBs, including their metrics in FZ are given in the Supporting Information.

LAMMPS [79] simulations are used to generate GB structures at zero temperature and pressure in a periodic box ($l_z \approx 2 \times \max(l_x, l_y)$ for LAGBs; $l_z = 20a$ for HAGBs) following the sampling method of Homer et al. [63]. In total, 26.8 million structures are examined for 5344 GBs (4864 mixed, 256 symmetric tilt and 224 twist GBs). To the authors' knowledge, this number, as well as the GB size and structural richness that it represents have shown an order of magnitude greater than most of the reviewed minimum GB energy datasets [11, 14, 28, 30, 32–35, 43–45, 60].

Only classical interatomic potentials could minimize so many GB structures within acceptable costs. The authors adopted a modified Tersoff potential [80], which not only reproduces the elastic constants and generalized stacking fault energies of silicon but is also proven capable of modelling complex atomic bond environments and dislocation structures [66]. First-principles calculations and the involved methods [81–84] are used for parallel comparisons with atomistic simulations. The details are given in the Supporting Information.

The dislocation analysis tool (DXA) implemented in the software Ovito [85, 86] is used to identify dislocations structured LAGBs, setting the trial Burgers circuit length to 9 atom-to-atom steps and a default Burgers vector circuit stretchability.

GB energy E^{Total} from atomistic simulation and first-principles calculation are defined as the following:

$$E^{\text{Total}} = \frac{\sum_i^N \left(E_i - E_{\text{Coh}} \right)}{A_{\text{GB}}} \tag{1}$$

Where N is the atom count of a GB in the simulation box (usually half of the box atoms because a box contains two GB). E_i is the energy of atom i, $E_{\text{Coh}} = -4.63\text{eV}$ is the cohesive energy of silicon atoms [87] and A_{GB} is the GB area. The Virial stress tensor of each atom is computed to show stress fields.

3. Results & Discussions

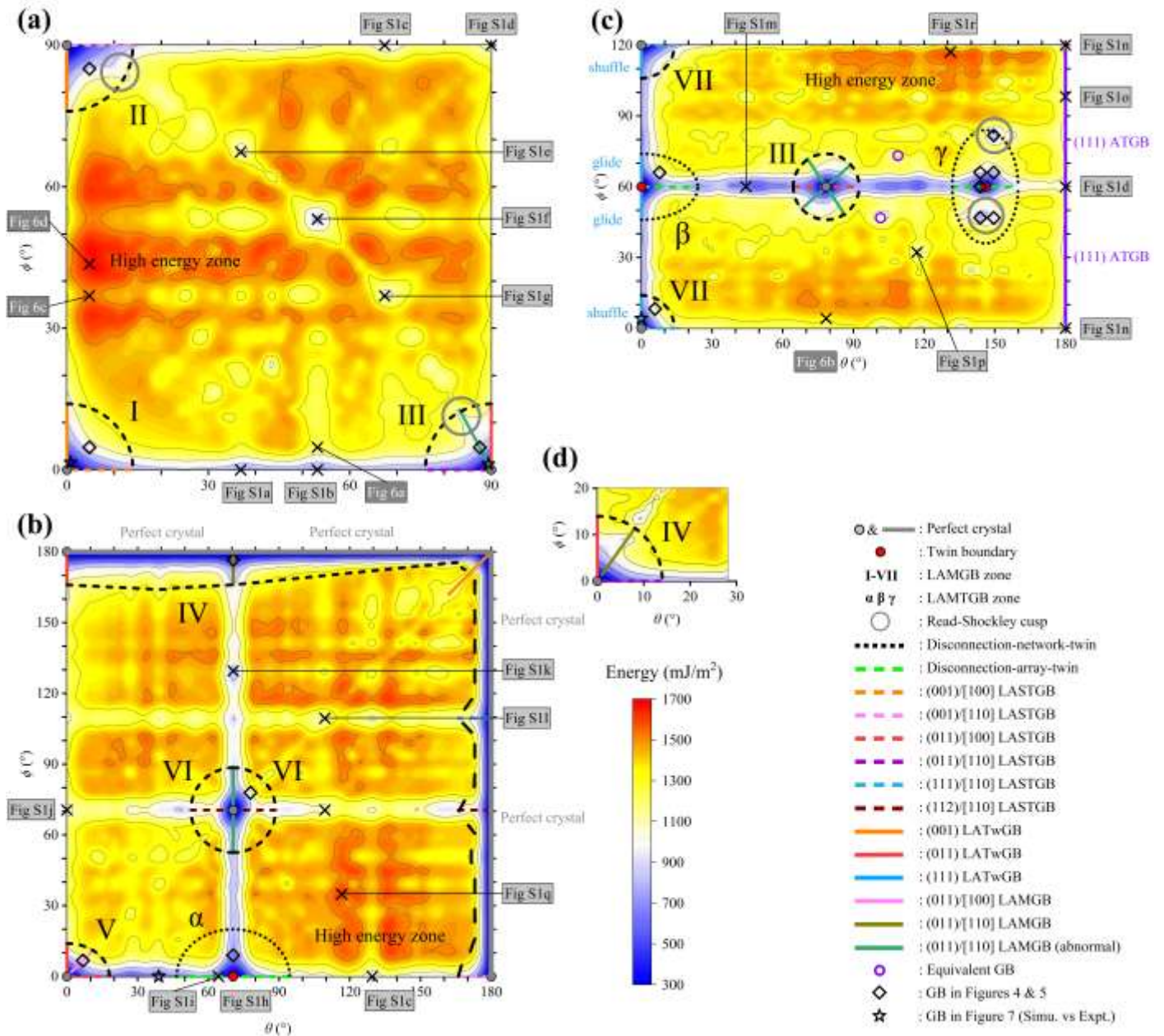## 3.1. Grain Boundary Energy

3.1.1. Energy surface

Figure 2. Energy surfaces of the examined mixed GBs as the functions of the tilt and twist angles. (a) (001)/[100] mixed GB; (b) (011)/[100] mixed GB; (c) (111)/[110] mixed GB; (d) low angle portion of (011)/[110] mixed GB. The mixed character space is non-Euclidean, and thus zone IV of (011)/[100] mixed GB in (b) is the expansion of the counterpart of (011)/[110] mixed GB in (d). Even in the LAMGB zones where the dislocation density is proportional to the tilt and twist angles, one should notice that the energy trends are not completely smooth and show Read-Shockley cusps.

Figures 2a, 2b and 2c show the (001)/[100], (011)/[100], (111)/[110] mixed GB energies as a continuous function of tilt angle θ and twist angle ϕ, respectively. Inspection of GB structures indicates that all GB energy surfaces can be divided into two parts, low angle mixed grain boundaries (LAMGBs) comprised of dislocation network structures (also include low angle mixed twin grain boundaries (LAMTGBs, disconnection network structures on twin GB) and high angle mixed grain boundaries (HAMGBs) comprised of amorphous structures,

which are divided by the black dash line and named as the LAMGB, LAMTGB, and HAMGB zones, respectively.

We first consider the seven unique LAMGB zones I to VII and the three unique LAMTGB zones α, β and γ, where the energy trends follow the Read-Shockley relationship. The ten zones are supposed to have elliptic shapes and some only show a quarter or a half due to the symmetry. LASTGB, LATwGB and disconnection-array-twin (DAT) structures are observed passing through the perfect crystal and twin GBs, and they represent the parts of the common 1D symmetric tilt or twist subsets that are frequently reported [11, 13, 14, 30, 32, 42–45, 69, 70]. The elliptic long and short axes that define the ten LAMGB and LAMTGB zones are determined by the core radius of dislocations in these LASTGBs, LATwGBs and DAT structures (i.e., dislocation core radius determines the curvature of each elliptic zone), where detailed explanation of such fact is referred to the authors' previous work.

For the HAMGB zones, there are various energy peaks which distributions form band-like landscapes (marked as the high energy zones in Figure 2), along with numerous energy cusps that are distributed separately. The complexity of the three energy surfaces makes the modern GB energy functions that extrapolate from existing 1D subsets [88, 89] very difficult to predict the energy cusps therein. Beyond this, the energies of most HAMGBs are very close to the average energy of all examined GBs at around 1340 mJ/m^2, a quite high value because most simple silicon HASTGB energies are located at $\sim$ 800 mJ/m^2. One may also wish to predict the positions of energy cusps in the energy surface. By decomposing the mixed GBs into pure tilt and twist components, a rough correlation could be found between low energy HAMGB and low energy HASTGB/HATwGB. However, it is only a kind of preliminary observation while quantitative correlation is still difficult to extract. For each energy surface, detailed descriptions are given in the Supporting Information.
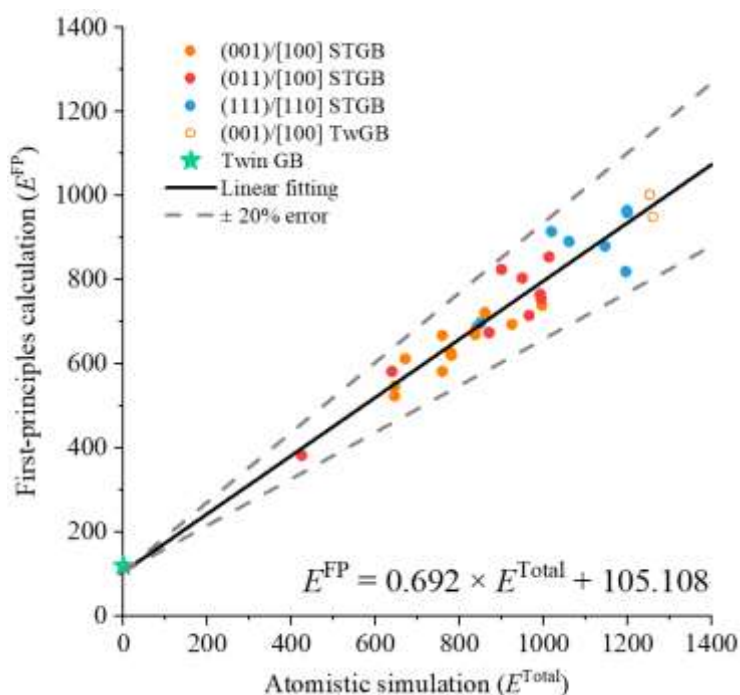
3.1.2. First-principles calculation

Figure 3. Comparison of calculated GB energies between atomistic simulation and first-principles calculation. Energy from

atomistic simulation E^{Total} and energy from first-principles calculation E^{FP} follows the linear relationship $E^{FP} = 0.692 \times E^{Total} + 105.108$.

To validate the presented energy surface, GBs with low Σ values that fall in the acceptable computational range are submitted to the first principles calculation. While the atomistic simulation reports nearly zero energy (0.04 mJ/m^2), the first principles calculation gives twin GB energy at 119.55 mJ/m^2, both of which agreed with the published data of silicon and carbon [45]. The simulated energy is in good linear scaling with the first-principles calculation (falls in ± 20% error lines), and suggests that the computed energy surface is reliable and can be extrapolated to first-principles results via the linear relationship in Figure 3. Also, this fact indicates that similar trends of the energy surface will be observed if more accurate (but consuming) computational methods are deployed.

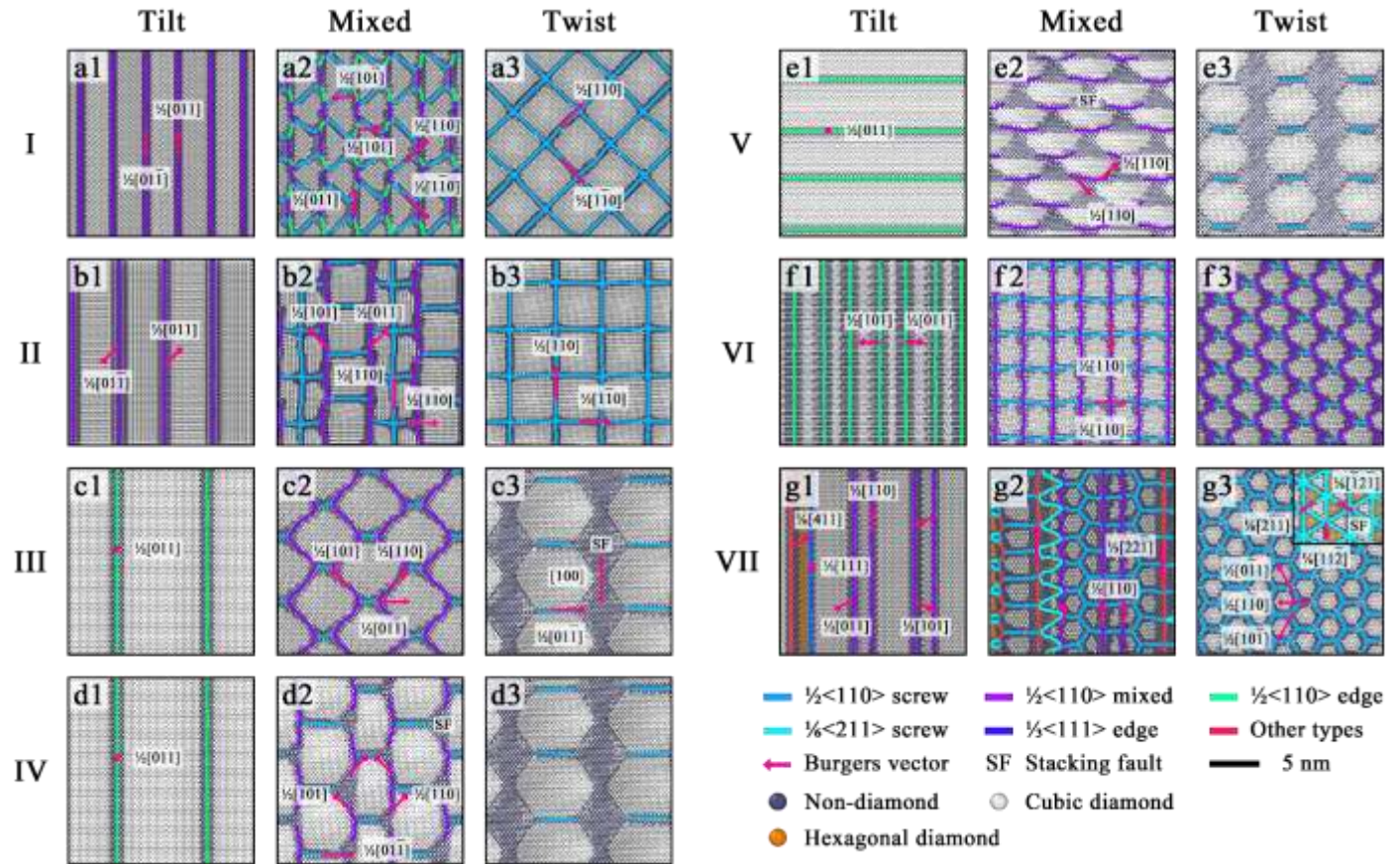## 3.2. Grain Boundary Structure

3.2.1. Dislocation structures

Figure 4. Dislocation structures of low angle symmetric tilt, twist and mixed GBs in the LAMGB zones I to VII of Figure 2. (a1) $\theta = 4.77°$ (001)/[100] LASTGB; (a2) $\theta = 4.77°$, $\phi = 4.77°$ (001)/[100] LAMGB; (a3) $\phi = 4.77°$ (001) LATwGB; (b1) $\theta = 3.38°$ (001)/[110] LASTGB; (b2) $\theta = 3.38°$, $\phi = 4.77°$ (001)/[110] LAMGB; (b3) $\phi = 4.77°$ (001) LATwGB; (c1) $\theta = 2.43°$ (011)/[110] LASTGB; (c2) $\theta = 2.43°$, $\phi = 3.39°$ (011)/[110] abnormal LAMGB; (c3) $\phi = 3.39°$ (011) LATwGB; (d1) $\theta = 2.43°$ (011)/[110] LASTGB; (d2) $\theta = 2.43°$, $\phi = 3.39°$ (011)/[110] LAMGB; (d3) $\phi = 3.39°$ (011) LATwGB; (e1) $\theta = 4.50°$ (011)/[100] LASTGB; (e2) $\theta = 4.50°$, $\phi = 4.50°$ (011)/[100] LAMGB; (e3) $\phi = 4.50°$ (011) LATwGB; (f1) $\theta = 7.91°$ (112)/[110] LASTGB; (f2) $\theta = 7.91°$, $\phi = 6.38°$ (112)/[110] LAMGB; (f3) $\theta = 4.51°$, $\phi = 6.38°$ (011)/[110] abnormal LAMGB (mixed GB as the twist component); (g1) $\theta = 5.84°$ (011)/[100] LASTGB; (g2) $\theta = 5.84°$, $\phi = 8.26°$ (011)/[100] LAMGB; (g3) $\phi = 8.26°$ (011) shuffle LATwGB (the glide variant is in the small sub-figure);

Dislocation structures of seven LAMGBs in the LAMGB zones I to VII are shown in Figure 4, where all LASTGBs and LATwGBs are dislocation arrays and dislocation network (the (011) LATwGB is a hybrid dislocation and stacking fault network), respectively. Meanwhile, the topology of both the dislocation array and network would not change once the ratio between the tilt and twist angles (tilt-twist ratio, *TTR*) is determined. Such two facts depend on the inherent geometry definition of LAGBs (transferable among materials), which are acknowledged by these works [67, 68, 74]. Formation mechanisms of the seven LAMGBs (Figures 4a2 to 4g2) can be considered as the superposition of their tilt components (Figures 4a1 to 4g1) and twist components (Figures 4a3 to 4g3) after energetically favorable dislocation glide and reaction. The authors marked the types and Burgers vectors of each dislocation segment to make the glide and reaction easily traceable. In most LAMGBs, the dislocation glide and reaction mechanisms are based on ½<110> screw dislocation, shown in Figures 4a2, 4b2, 4d2. The ½<110> screw dislocation suffered segmentation from ½<110> mixed dislocation, and then glide half of the spacing. There are more complex mechanisms involving the stacking fault from (011) LATwGB in Figures 4c2, 4d2 and 4e2. ½<110> edge dislocations in Figures 4d1 and 4e1 separate both stacking fault (equivalent to a <100> Burgers vector) and ½<110> screw dislocation of (011) LATwGB in two different orientations, which finally yields two different LAMGBs in Figures 4d2 and 4e2. Although the mechanisms governing (011) LAMGB structures are complicated and involve stacking fault, it indeed follows the same as the (001) LAMGB once the stacking fault is approximately considered as a dislocation. Even in the complex (111)/[110] LAMGB of Figure 4g2, the generation of the uncommon ⅙<411> mixed and ⅓<221> mixed dislocations are also caused by the dislocation reactions that including ½<110> screw dislocation.

It should be noted that two LAMGB zones are been considered special or abnormal. The first is zone III, where all LAMGBs do not contain infinite, straight dislocation lines. The dislocation reaction is the same with the LAMGBs in zone IV, but the ½<110> mixed dislocation glides to the edge of the stacking fault area and forms a zigzag pattern. LAMGB zone III decomposes exactly into the same tilt and twist components as zone IV. However, zone III cannot be indexed by examining the (011)/[110] energy surface in Figure 2, instead, it can be indexed by examining the (001)/[100] energy surface. The second zone is VI because its decomposed twist component is LAMGB in zone III rather than LATwGB. LAMGBs in zone VI is the superposition of (112)/[110] LASTGB and (011)/[110] LAMGB where the LAMGB plays the role of twist component.
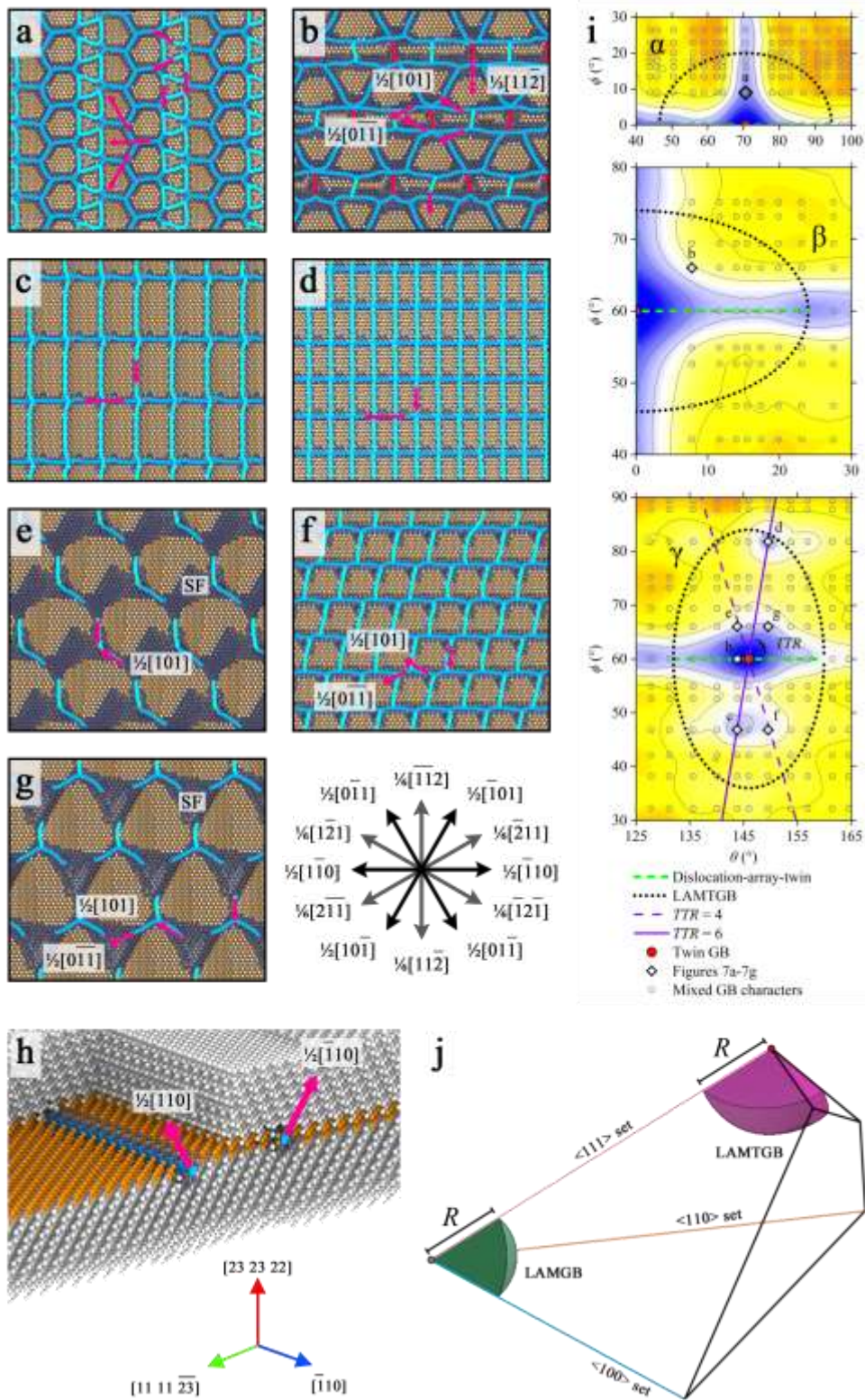
Figure 5. Disconnection network structures in the LAMTGB zones α, β and γ of Figure 2. (a)-(g) 2D planar view of the LAMTGB structures; (h) 3D view of a DAT structure, showing a step of twin layer; (i) Distance to twin GB of (a)-(h). (j) Proportions of LAMGB and LAMTGB in the Rodriguez-Frank space. LAMGB and LAMTGB portions of the Rodriguez-Frank space can be approximated as a spherical pyramid with radius *R*, where *R* is determined by the average dislocation core radius [66, 69]. Explanations of symbols follow the same in Figure 4.

Figure 5 shows the disconnection structures of eight LAMTGBs (from zones α, β and γ), which are formed by introducing low misorientations on twin GB. A major difference between LAMTGB and LAMGB is that the LAMTGB is difficult to decompose into tilt and twist components. For example, if we assume that

its tilt component is the twin GB while its twist component is the attached disconnection network, then it will contradict the fact that twin GB also plays as a twist component in Figure 2b. Beyond this fact that confuses the GB decomposition, the LAMTGBs in the three zones share a common feature with the LAMGB. It is that the topology of the dislocation/disconnection network does not vary with the parameter TTR, which is proven by comparing LAMTGBs in Figures 5c and 5d that are located on the $TTR = 6$ lines in Figure 5. In summary, it can be seen that the twin GB could also accommodate complex disconnection structures, and the role of the twin GB is just like the perfect crystal in the mixed character space, as illustrated in Figure 5i. This is because the mixed GB characters near the twin GB are disconnection structures which topology depends on the parameter TTR. Although the formation mechanisms and the decomposition criterion of the LAMTGBs should be further explored, the authors are still optimistic about these results and conclusions as they show promising capability for interface engineering and self-assembled nanostructures.

3.2.2. Amorphous structures

Atomic structures of four HAMGBs without dislocation core structures but with typical dislocation stress fields are plotted in Figure 6. Figure 6a1 is the atomic structures of a near Σ5 HAMGB generated by introducing a low twist angle ($\phi = 4.77°$) on the boundary plane normal of the well-known kite-shaped Σ5 STGB (Figure S1a). The upper view along its boundary plane normal in Figure 6a2 shows a squared shadow pattern, which follows the same spacing with the squared dislocation network of a $\phi = 4.77°$ (001) LATwGB. Stress fields of the HAMGB in Figure 6a3 are also similar to the dislocation stress fields of the LATwGB in Figure 6a5. Figure 6b1 is the atomic structures of a near Σ15 HAMGB generated by introducing a low twist angle ($\phi = 4.13°$) on the boundary plane normal of a Σ15 STGB. The HAMGB also generates different but considerable stress fields in Figure 6b3 as compared with its twist component, a $\phi = 4.13°$ (111) LATwGB in Figure 6b5. The differences in stress fields are from the superposition and mutual perturbation of the stress fields of HAMGB components. To verify such an explanation, two HAMGBs and their stress fields are given in Figures 6c1 and 6d1, where both tilt components are the $\theta = 4.77°$ (001)/[100] LASTGB (Figure 6c5). We can see that the stress fields of the two HAMGBs show the same stress characteristics compared with the dislocation stress fields in Figure 6c6, although both of them are completely amorphous structures without any identifiable dislocation core or SUs (i.e., SU is too big to be applicable, similar to the prediction of the very early inter-crystalline amorphous cement theory [90]). However, the dislocation stress fields shown in Figure 6c2 are more remarkable than the counterparts shown in Figure 6d2, which is explained by the complexity of their twist components. For instance, the (001) TwGB structures corresponding to the two HAMGBs are given in Figures 6c3 and 6d3. Obviously, the SU in Figure 6c3 has a lower size than the one in Figure 6d3, which simplifies SU stress characteristics and finally results in more remarkable dislocation stress fields.
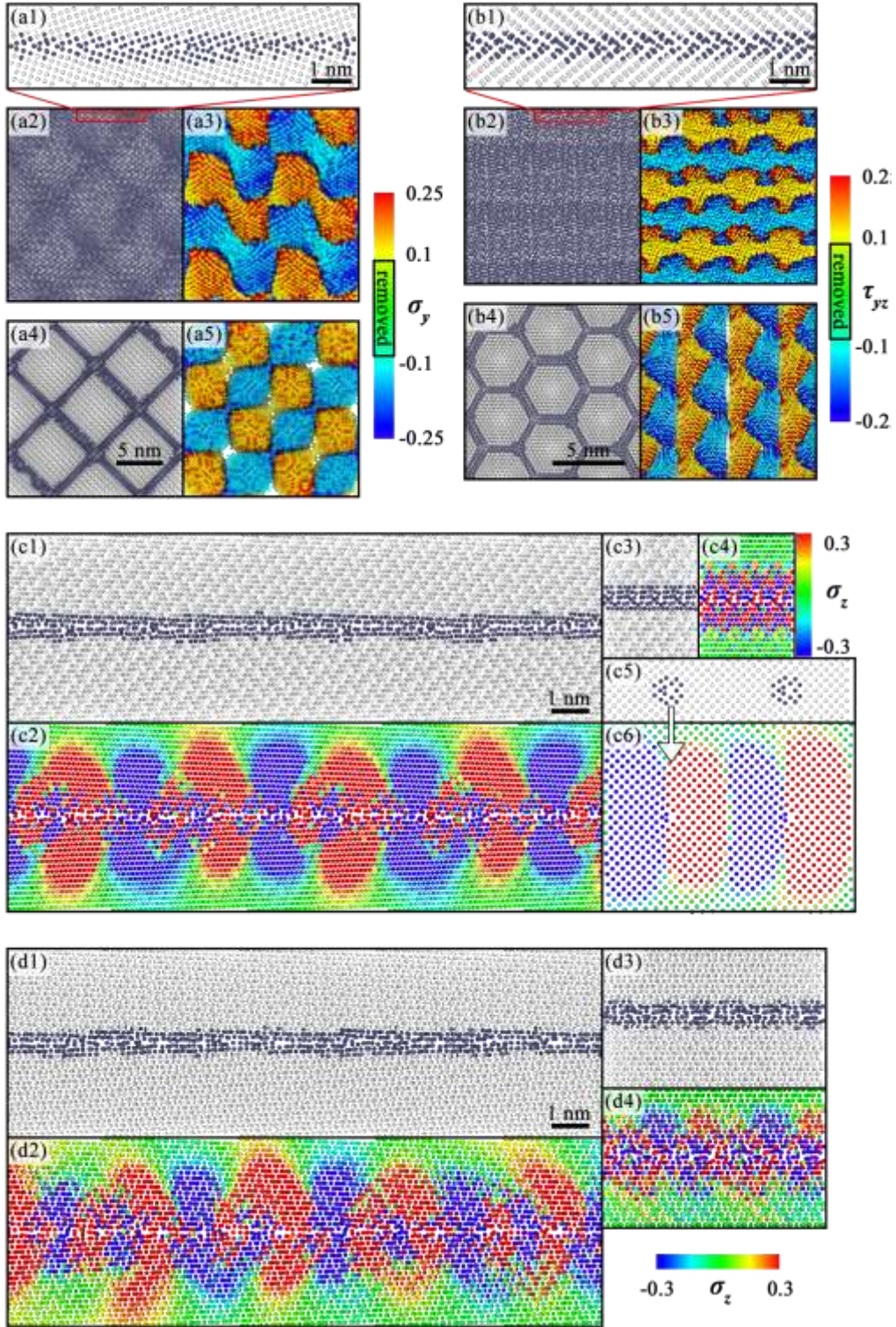
Figure 6. Atomic structures and stress fields of HAMGBs in Figure 2. (a1) Side view of atomic structures of a Σ26001 (288 12 577) HAMGB, which is formed by introducing a 4.77° twist angle on the $\theta = 53.13°$ Σ5 (102) STGB; (a2) Upper view of atomic structures of the Σ26001 (288 12 577) HAMGB; (a3) Upper view of distribution of stress component σ_y of the Σ26001 (288 12 577) HAMGB; (a4) Upper view of atomic structures of the $\phi = 4.77°$ (001) LATwGB (the same with Figure 4a3); (a5) Upper view of distribution of stress component σ_y of the (001) LATwGB; (b1) Side view of atomic structures of a Σ328363 (507 5 267) HAMGB, which is formed by introducing a 4.13° twist angle on the $\theta = 78.46°$ Σ15 (201) STGB; (b2) Upper view of atomic structures of the Σ328363 (507 5 267) HAMGB; (b3) Upper view of distribution of stress component τ_{yz} of the Σ328363 (507 5 267) HAMGB; (b4) Upper view of atomic structures of the $\phi = 4.13°$ (111) LATwGB; (b5) Upper view of distribution of stress component τ_{yz} of the (111) LATwGB; (c1) Side view of atomic structures of a Σ3605 (2 1 60) HAMGB, which is formed by introducing a 4.77° tilt angle on the $\phi = 36.87°$ Σ5 (001) TwGB; (c2) Side view of distribution of stress

11

component σ_z of the $\Sigma3605$ (2 1 60) HAMGB; (c3) Side view of atomic structures of a $\phi = 53.13°$ $\Sigma5$ (012) TwGB; (c4) Side view of distribution of stress component σ_z of the $\phi = 53.13°$ $\Sigma5$ (012) TwGB; (c5) Side view of atomic structures of a $\theta = 4.77°$ (001)/[100] LASTGB; (c6) Side view of distribution of stress component σ_z of the $\theta = 4.77°$ (001)/[100] LASTGB; (d1) Side view of atomic structures of a $\Sigma485141$ (25 10 696) HAMGB, which is formed by introducing a 4.77° tilt angle on the $\phi = 43.60°$ $\Sigma29$ (025) TwGB; (d2) Side view of distribution of stress component σ_z of the $\Sigma485141$ (25 10 696) HAMGB; (d3) Side view of atomic structures of a $\phi = 43.60°$ $\Sigma29$ (025) TwGB; (d4) Side view of distribution of stress component σ_z of the $\phi = 43.60°$ $\Sigma29$ (025) TwGB.

By comparing two cases 1) STGB accommodates a low twist component and 2) TwGB accommodates a low tilt component, it is found that the stress fields of any mixed GB with a low angle component are the superposition of its tilt and twist component's stress fields. Such superposition also depends on the structural complexity of the high angle tilt/twist GB as simpler SUs have higher capability to maintain the dislocation stress fields. These findings suggest that the energies of these amorphous GB structures are not completely from lattice disorder, the strain energy also plays a critical role, which could be further described in the framework of the classical Read-Shockley relationship.
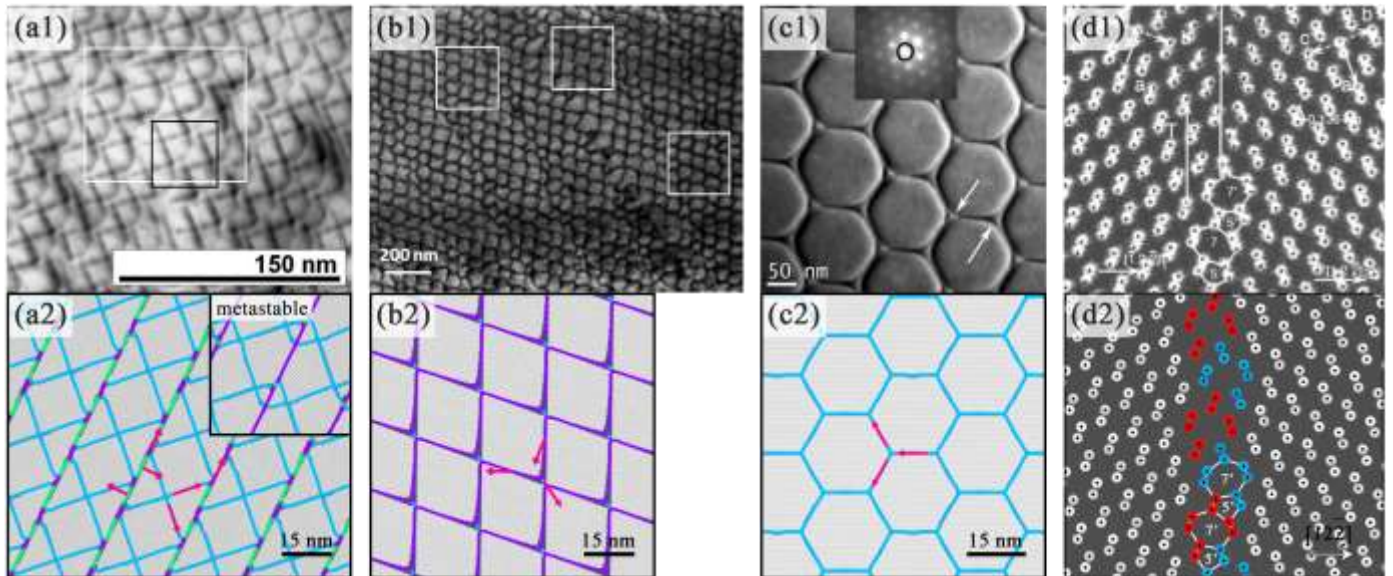
3.2.3. Comparison with experiments

Figure 7. Comparisons between experimental observations and atomistic simulations. (a1) Experimental observation of a (001) LAMGB from Wilhelm et al. [77]; (a2) 1:1 simulation reproduction of the (001) LAMGB structures at the stable state, the subfigure indicates a meta-stable state of the (001) LAMGB structures; (b1) Experimental observation of a (011) LAMGB from Reiche et al. [91]; (b2) 1:2.66 simulation reproduction of the (011) LAMGB structures at the stable state. The comparison mainly focuses on the dislocation network topology as the dislocation spacing is proportional to both θ and ϕ; (c1) Experimental observation of a (111) LATwGB from Neily et al. [72]. The hexagonal dislocation network shows partial dissociation to triangular hybrid dislocation and stacking fault at the dislocation triple junctions; (c2) 1:7 simulation reproduction of the (111) LATwGB structures at the stable state. The stable (111) LATwGB has hexagonal dislocation network structures that correspond to the (111) shuffle plane, while the triangular hybrid dislocation and stacking fault structures of the (111) glide plane are metastable; (d1) Experimental observation of a (011) HASTGB from Bonnet, et al. [92]; (d2) 1:1 simulation reproduction of the (011) HASTGB structures at the stable state. The error of each atom position is less than 0.01 nm.

Figure 7 shows the comparisons between experimental observations and atomistic simulations of four silicon GBs. The positions (in the mixed character space) of the simulated GBs 7a2, 7b2, 7c2 and 7d2 used in

comparison have been marked in Figure 2. It is surprising that the simulation shows the unique capability to accurately reproduce both dislocation and amorphous silicon GB structures at the atomic level. For example, the experiments versus simulation is 1:1 in the length scale for GBs in Figures 7a and 7d. The simulation reproduces the complex topology of the dislocation network across the nano-scale, and even the meta-stable dislocation network structures partially shown in Figure 8a1 are captured, which is given in the subfigure of Figure 7a2. The success demonstrates that the simulated dislocation structures in Figure 4 are reliable. Meanwhile, for the LAMGBs shown in Figures 7b1 and 7c1, the comparisons should be addressed on the fact that dislocation network topology does not vary with *TTR*. The fact allows us to reproduce the experimentally observed LAMGB structures in a designated scale like 1:2.66 or 1:7, rather than 1:1 reproduction that makes the computational resources unbearable. The presented simulation agreed well with the experimentally observed (011) LAMGB and the (111) LATwGB, but the atomistic simulation at zero temperature and pressure fails to capture the dislocation dissociation at the triple junctions of (111) LATwGB at the finite temperatures. It is acceptable as the simulation predicts the (111) shuffle LATwGB (hexagonal ½<110> screw dislocation network) is the stable state rather than the (111) glide LATwGB (triangular hybrid ⅙<211> screw dislocation and stacking fault network) with slightly higher energy. Detailed understandings of the difference and mutual conversion between (111) shuffle and glide planes in silicon and FCC metals are referred to in these works [45, 93, 94]. For the structural unit GB shown in Figure 7d1, the simulation in Figure 7d2 gives an unexpected excellent agreement, the error of each atom position is sub-angstrom level. In summary, the comparisons between experiment and simulation proved that the simulation method and results are reliable for the full range of GB structures, and further verifies the conclusion that the LAMGBs are indeed the superposition of their tilt and twist components.

3.3. A universal Read-Shockley model

3.3.1. Theorization

On the basis of the presented discussions, a general framework that is universal for the structures and energies of mostly GBs spanning the mixed character space is presented. First of all, we summarized a qualitative estimation strategy of the structures, energies and stress fields of a given mixed GB from its decomposed components in Figure S2, which would be useful in the preliminary analysis. Then, we started quantifying the mixed GB energy from the LAMGB, which energy is usually divided into the dislocation core and strain energies. As Wan and Tang have mentioned, the dislocation core energy is equal to the sum of the dislocation core energy of both LAMGB tilt and twist components minus the loss of dislocation core energy from dislocation reactions [66]. For the dislocation strain energy, a mutual perturbation between the stress fields of LAMGB tilt and twist components is expected. In that case, LAMGB energy E could be written as the function of θ and ϕ following

$$E_{\text{LAMGB}}^{\text{Total}}(\theta,\phi) = E_{\text{LASTGB}}^{\text{Total}}(\theta) + E_{\text{LATwGB}}^{\text{Total}}(\phi) + E_{\text{Loss}}^{\text{Core}} + E_{\text{Loss}}^{\text{Strain}} \tag{2}$$

Where superscript Total, Core and Strain denote the LAMGB excess energy, dislocation core and strain energies, respectively. Subscript LAMGB, LASTGB and LATwGB denote the GB type. Subscript Loss denotes the energy loss from the dislocation glide and reaction process. Equation (2) is purely a qualitative

expression. Read and Shockley have already given the analytical expression of the LASTGB and LATwGB energies known as the classical Read-Shockley relationship ($\theta - \theta\ln(\theta)$ and $\phi - \phi\ln(\phi)$) for the first two terms of equation (2), but note that the detailed expressions within the last two terms are still unclear. An empirical expression of the last two terms of equation (2) has been proposed by Wan and Tang [66], which is called the revised Read-Shockley relationship following:

$$E_{\text{LAMGB}}^{\text{Total}}(\theta,\phi) = \theta\left[E_{\text{LASTGB}}^{\text{Core}} - E_{\text{LASTGB}}^{\text{Strain}}\ln(\theta)\right] + \phi\left[E_{\text{LATwGB}}^{\text{Core}} - E_{\text{LATwGB}}^{\text{Strain}}\ln(\phi)\right] +$$
$$\theta\phi\left[E_{\text{Loss}}^{\text{Core}} - E_{\text{Loss}}^{\text{Strain}}\ln(\theta\phi)\right] \tag{3}$$

Where the last two terms $E_{\text{Loss}}^{\text{Core}} + E_{\text{Loss}}^{\text{Strain}}$ that follow the Read-Shockley formalism $\theta\phi - \theta\phi\ln(\theta\phi)$ are considered to have a good balance of both fitting effects and clarity [66]. It agrees with the prediction of Sutton and Balluffi that any LAMGB structure-energy relationships should follow or be similar to the Read-Shockley formalism. The compatibility of equation (3) is strong. For example, by replacing θ and ϕ with $\sin(\theta)$ and $\sin(\phi)$, Equation (3) becomes the Wolf's version of the Read-Shockley relationship [95]. Equation (3) can accommodate an additional energy term E_i to describe the interaction of the dislocation network of LATwGB, as Vitek did [96]. LAMTGBs also follow the same dislocation glide and reaction mechanisms as the authors previously described for LAMGBs. Since the LAMTGBs are disconnection structures on the twin GB, an additional twin GB energy term E_{Twin} must be appended to equation (3) to capture the energy trends in the LAMTGB zone following:

$$E_{\text{LAMTGB}}^{\text{Total}}(\theta,\phi) = \theta\left[E_{\text{LASTGB}}^{\text{Core}} - E_{\text{LASTGB}}^{\text{Strain}}\ln(\theta)\right] + \phi\left[E_{\text{LATwGB}}^{\text{Core}} - E_{\text{LATwGB}}^{\text{Strain}}\ln(\phi)\right] +$$
$$\theta\phi\left[E_{\text{Loss}}^{\text{Core}} - E_{\text{Loss}}^{\text{Strain}}\ln(\theta\phi)\right] + E_{\text{Twin}} \tag{4}$$

Equation (3) and its variants are not only applicable for dislocation structured and disconnection-twin structured GBs but also available for some amorphous mixed GB structures containing a low angle tilt/twist component. The mixed GB with typical dislocation stress shown in Figure 4 is a good example. Hence, if we introduce a small twist angle ϕ on a HASTGB ($\theta = \theta_1$) or a small tilt angle θ on a HATwGB ($\phi = \phi_1$), then for the corresponding HAMGBs, equation (3) varies to

$$E_{\text{HAMGB}}^{\text{Total}}(\theta_1,\phi) = E(\theta_1,0) + \phi\left[E_{\text{LATwGB}}^{\text{Core}} - E_{\text{LATwGB}}^{\text{Strain}}\ln(\phi)\right] +$$
$$\theta_1\phi\left[E_{\text{Loss}}^{\text{Core}} - E_{\text{Loss}}^{\text{Strain}}\ln(\theta_1\phi)\right] \tag{5}$$

and

$$E_{\text{HAMGB}}^{\text{Total}}(\theta,\phi_1) = \theta\left[E_{\text{LASTGB}}^{\text{Core}} - E_{\text{LASTGB}}^{\text{Strain}}\ln(\theta)\right] + E(0,\phi_1) +$$
$$\theta\phi_1\left[E_{\text{Loss}}^{\text{Core}} - E_{\text{Loss}}^{\text{Strain}}\ln(\theta\phi_1)\right] \tag{6}$$

respectively. Once the known terms are eliminated, the straightforward forms of equations (5) and (6) could be written as

$$E_{\text{HAMGB}}^{\text{Total}}(\theta_1,\phi) = E(\theta_1,0) + \phi\left[E^{\text{Core}} - E^{\text{Strain}}\ln(\phi)\right] \tag{7}$$

and

$$E_{\text{HAMGB}}^{\text{Total}}(\theta,\phi_1) = \theta\left[E^{\text{Core}} - E^{\text{Strain}}\ln(\theta)\right] + E(0,\phi_1) \tag{8}$$

respectively. Where E^{Core} and E^{Strain} are fitting terms in the classical Read-Shockley relationship [46]. Equations (7) and (8) have constraints that the GB energies at finite temperatures are incapable of exceeding

a maximum value E_{max} (maximum lattice distortion in the 5D GB space), no matter how the GB macroscopic and microscopic DOFs change.
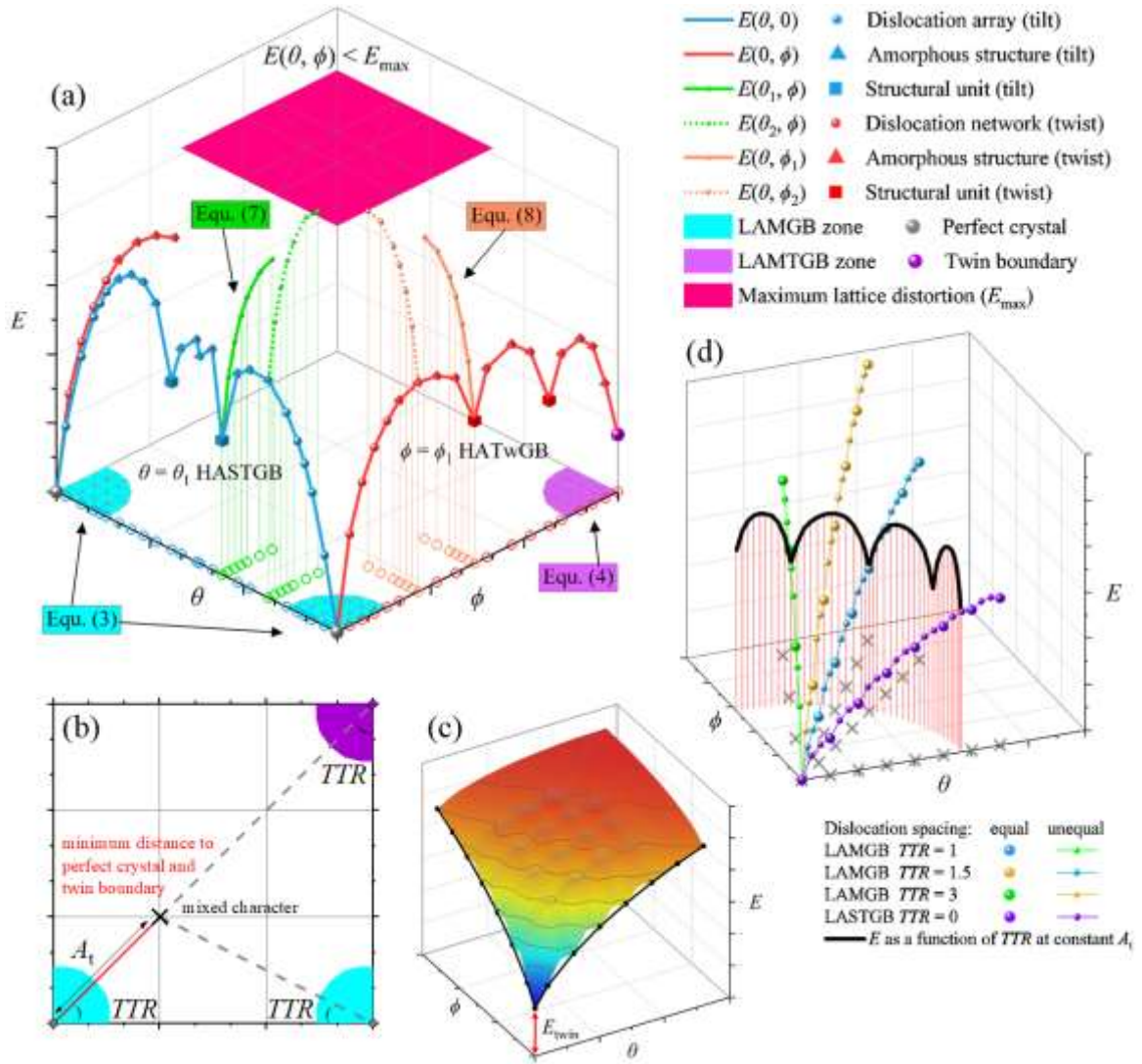

Figure 8. Conceptualization and illustration of the universal Read-Shockley GB energy model in the mixed character space. (a) Assumed energy trend in an assumed mixed character space; (b) Definition of the total misorientation angle in the mixed character space; (c) Assumed 2D energy surface in an assumed LAMGB zone; (d) Assumed GB energy trends in an assumed LAMGB zone as a 2D extension of the 1D Read-Shockley relationship [46]. Note that all data in Figure 10 is not real due to the illustration purpose.

Equations (2) to (8) and the relevant discussions are summarized in Figure 8a as a universal Read-Shockley model for GB energies spanning the mixed character space. Figure 8b shows the definition of the total misorientation angle A_t in the mixed character space. Unlike the frequently used conventional definition of misorientation angles in the Rodriguez-Frank space, A_t of a mixed GB character is defined as its minimum angular distances to the positions of all perfect crystals and twin GBs in a given mixed character space following:

$$A_t = \sqrt{\theta_{min}^2 + \phi_{min}^2}$$ (9)

Where θ_{min} and ϕ_{min} are defined as the minimum tilt and twist angular distances to the positions of all perfect crystals and twin GBs, respectively. Such a definition allows us to adapt the fact that the dislocation/disconnection network topology of both LAMGBs and LAMTGBs is governed by the parameter

TTR. Also, it guarantees that all dislocation/disconnection-structured GBs have low A_t values and are considered LAGBs.

Figure 8c shows an assumed energy surface in an assumed LAMTGB zone. The assumed energy surface is not smooth, on the contrary, they are full of deep cusps and high peaks, and equation (4) is only valid for the deep cusps where the dislocations are assumed with equal spacing and two components satisfy designated *TTR*. To make the explanation impressive, the authors plotted the assumed energy trends along several specific trace lines in an assumed LAMGB zone of Figure 8d. For a give trace line (*TTR* = constant), all LAMGBs will share the same dislocation network topology, but unequal dislocation spacing and/or additional dislocations would appear in most of them and generate high peaks, as highlighted by Read and Shockley [46] and double confirmed by Figure 4g1. However, the role of parameter *TTR* is beyond the expectation of Read and Shockley. For example, when tilt and twist components do not satisfy the designated *TTR*, excess dislocations (and/or stacking faults) are generated and then cause significant peaks between two trace lines with designated *TTR* (where two components are perfectly mixed without excess dislocations). Such a process is illustrated in the black energy line on the trace line with the same A_t value in Figure 8d. We must note that the energy contribution of the excess dislocations from the parameter *TTR* is always greater than the energy contribution of the unequal dislocation spacing. In other words, GB energy suffers low and high peaks in the 1) direction towards the perfect crystal and 2) the direction tangents to 1), respectively.
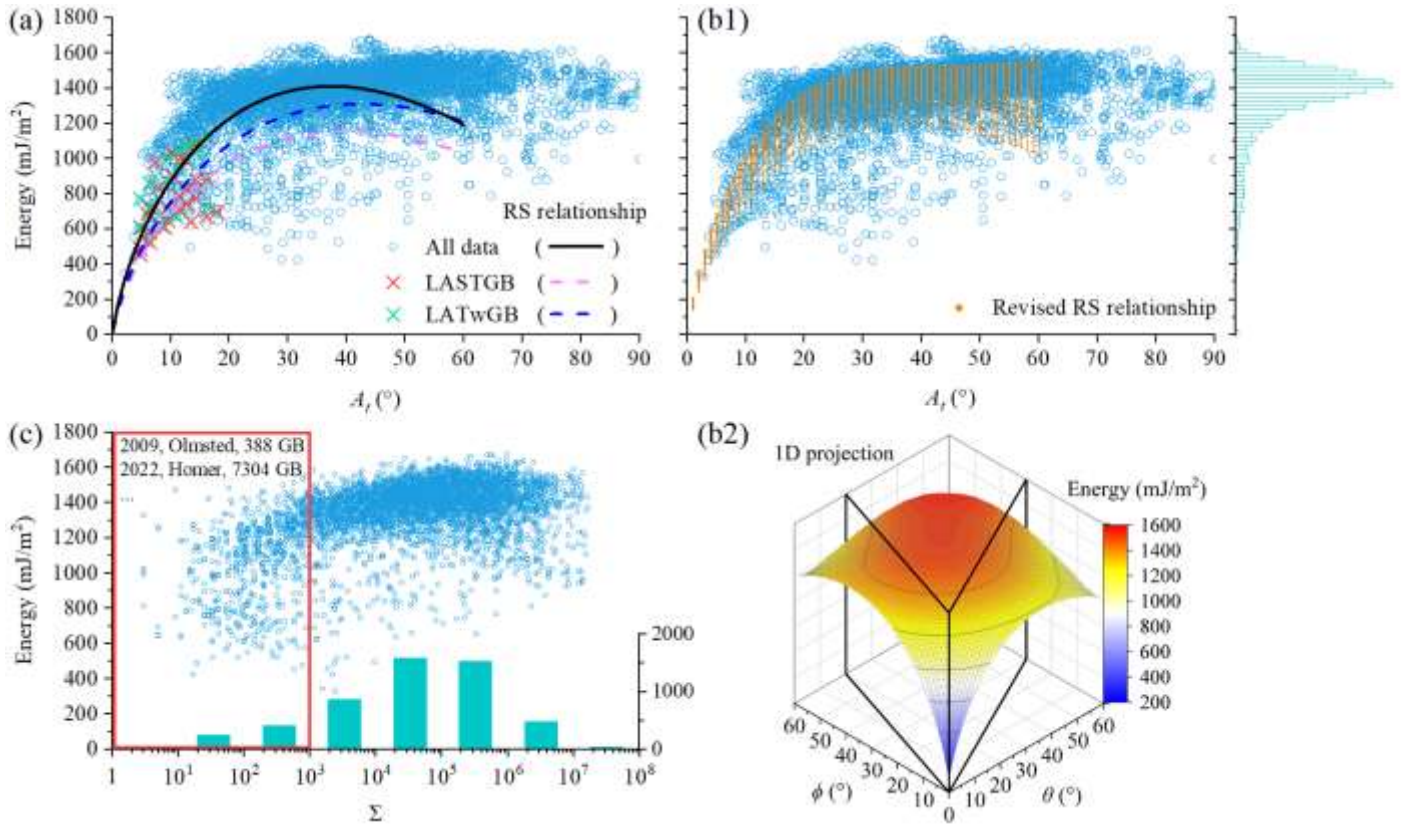
3.3.2. Performance & Transferability

Figure 9. Silicon GB energy against the selected scalars. (a) Silicon GB energy against the total misorientation angle A_t, and the fitting from the Read-Shockley (RS) relationship. All fittings only used data within 60°; (b1) Fitting of the mixed GB energy from the revised Read-Shockley relationship, plotted by projecting the two-dimensional energy surface of (b2) to one-dimension; (b2) Two-dimensional energy surface from the revised Read-Shockley relationship. Fitting parameters are given in Tables S7 and S8; (c) Silicon GB energy against Σ. It indicates that GB energy is gradually approaching a constant value

when Σ is higher than 10^3.

The performance of the universal Read-Shockley model is examined on the general characteristics of the silicon mixed GB dataset. The starting point is to convert the three energy surfaces to the one-dimensional simplification (indexed by parameter A_t). Figure 9a shows silicon GB energy as a function of A_t, accompanied by the marks of the LAGBs and the three fittings from the classical Read-Shockley relationship (Fittings of all GB, LASTGB and LATwGB energies. Fitting parameters are given in Table S9). The fitted trends of the mixed GB energy follow the classical Read-Shockley relationship, but are slightly higher than the fitted trends of both LASTGB and LATwGB. Figure 9b1 shows the fitting of all GB energies from equation (3), by converting the fitted 2D energy surface in Figure 9b2 via the introduced simplification. Compared with the classical Read-Shockley relationship, the revised Read-Shockley relationship shows natural superiority to fit so massive data as its one-dimensional simplification is a cloud-like distribution showing the range of GB energy at any A_t or misorientation angles. However, such simplification also suffers two obvious shortages: 1) The value of A_t may be higher than the constrain of the Rodriguez-Frank space as the mixed GB characters are simplified individually in each energy surface; 2) A given GB character is being indexed multiple times in different energy surfaces and no assurance of the uniqueness.

Figure 9c shows silicon GB energy as a function of Σ. The average Σ is approximately 4.4×10^5, and most of them are higher than 10^3, both of which imply the fruitfulness of GB atomic environments presented here. Note that the energies of high Σ HAMGBs (except for the low energy LAMGBs and LAMTGBs as both can be expressed with high Σ) are approaching 1400 mJ/m^2. A qualitative explanation is that these high Σ GBs are mostly amorphous structures without any SUs and dislocation structures that may contribute to low energy.
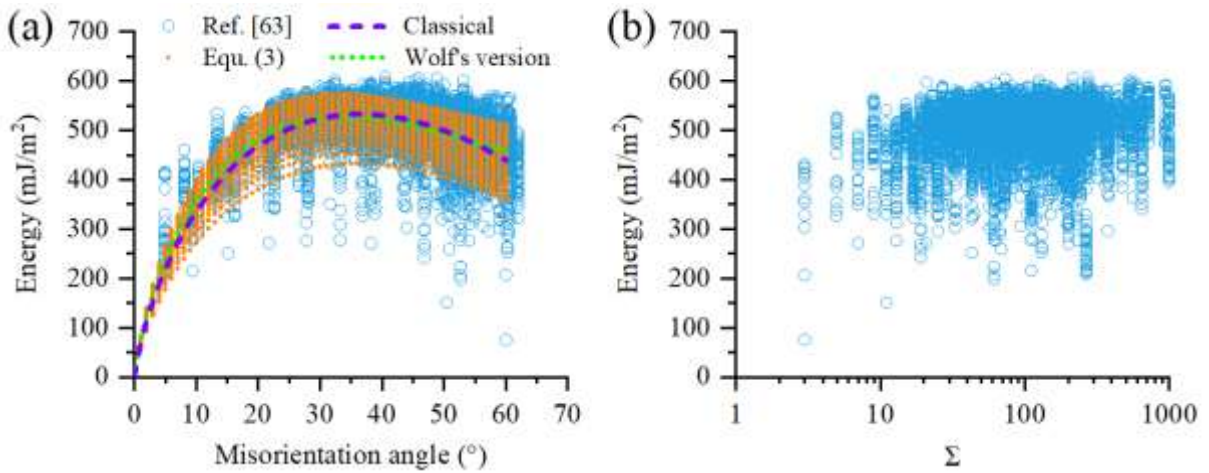

Figure 10. (a) 7304 aluminum GB energies versus the misorientation angle [63] (Rodriguez-Frank space definition). The purple dash line denotes fitting of the classical Read-Shockley relationship [46], and the green dash line denotes fitting of Wolf's version of the Read-Shockley relationship [92]. Fitting parameters are given in the Supporting Information; (b) 7304 aluminum GB energies versus Σ. Noting that authorization for the reuse of these published data has been obtained.

Figure 10 shows the fitting of the revised Read-Shockley relationship on a recently published aluminum GB dataset [63]. The fitting effects on aluminum GB are quite good because such relationship almost perfectly captures the general trends of aluminum GB energy compared with its original functional. The success of the revised Read-Shockley relationship in predicting both silicon and aluminum GB energy trends could also be extended to a wide range of materials across the FCC and diamond lattice through a key fact that GB energy

is scaling with the elastic modulus in the materials with the same lattice [97].

4. Conclusions

The energies and structures of 4964 silicon GBs with mixed tilt and twist characters, as well as their decomposed tilt and twist GB components are studied in this work to confirm whether the mixed GBs follow the principles of superposition. There are several conclusions worth noting:

- Structures and stress fields of a given mixed GB with a low angle tilt and/or twist component follow the principles of superposition: 1) Dislocation network structures (and stacking fault) of the LAMGBs are complex but predictable because they are formed by energetically favorable dislocation reaction and glide between LAMGB tilt and twist components; 2) Twin GB could accommodate complex disconnection network structures to form LAMTGB, while some simple SU GBs (e.g., Σ5 "kite" GB) show typical dislocation stress characteristics after introducing a low angle component, although they are completely amorphous structures. Qualitatively speaking, the principles of superposition are inversely correlated with both tilt and twist angles.

- A universal Read-Shockley model is proposed from a recently revised Read-Shockley relationship of Wan and Tang [66] on the basis of these reported structural features. This model accurately captures the energy trends of LAMGB and LAMTGB, and shows inherent superiority compared with the classical Read-Shockley relationship. Its universality is extracted by extending to those HAMGBs with a low angle component, while its transferability is proven by precisely fitting the energy trend of 7304 FCC aluminum GBs. As the supplementary of both classical Read-Shockley relationship and this model, we also highlighted the role of parameter *TTR* because the structures and energies of LAMGB and LAMTGB are especially sensitive to it.

- Experimental observed stable/metastable dislocation networks and atomic structures are reproduced by the simulation and thus validate the simulated GB structures and the derived conclusions. Notably, our work reports a sub-angstrom level error in atom positions while comparing the simulation and an experimentally investigated HASTGB, and thus makes the presented massive silicon GB structural datasets convincible. First-principles calculation on the energies of low Σ GBs is in good scaling with the atomistic simulation, which not only connects both simulation methods but further reinforces the reliability of the studied energetic properties.

In some cases, the principles of superposition on LAMGB structures are expected. However, we proved that this basic theory is not only limited to a variety of LAMGBs with different misorientation axes and boundary planes, and is even valid for amorphous GB structures in terms of stress fields and strain energies. In other words, dislocation and/or disconnection as the bridge connecting GBs that are crystallographic-close. Rugged trends of the energy surface formed by thousands of individual GB energy reinforce and extend the prediction of Read and Shockley decades ago, meanwhile, implying the unpredictable nature of HAMGB energy. The contributions of this work could be quite fundamental, it paved the way for understanding complex GB structures and designing interfacial patterns of self-assembled nanostructures.

Beyond these findings, more intriguing features could be explored further. Our work only addressed the

basic structural and energetic features of mixed GBs. It is uncertain whether the other GB properties (e.g., mobility, strength and thermal conductivity) follow the same formalism or are just simply non-linear. From the fundamental zone description of the presented GB dataset, it should be noted that the principles of superposition are only valid for the three GB DOFs associated with the misorientation axis and the superposition may work for different GB plane orientation fundamental zones. To fully understand the GB structure-property correlation across five macroscopic DOFs, more efforts are desired.

Data availability

Numerical data are available upon reasonable request.

Acknowledgements

Competing interests

The authors declare no competing interests.

Fundings

Author contributions

1) W. Wan carried out this project, provided the minor funding, performed all simulations, visualized all figures, theorized the universal Read-Shockley model, wrote the original manuscript and revised it.

2) C.X. Tang supervised the project, contributed computation resources, maintained the data, provided the major funding, and revised the manuscript.

3) E.R. Homer provided the fundamental zone description of the dataset, discussed the data, and revised the manuscript.

References

[1] Rubio, R.A.; Haouala, S.; Llorca, J. Grain boundary strengthening of FCC polycrystals. *J. Mater. Res.* **2019**, 34, 2263–2274.

[2] Zhou, Q.; Huang, P.; Liu, M.B.; Wang, F.; Xu, K.W.; Lu, T.J. Grain and interface boundaries governed strengthening mechanisms in metallic multilayers. *J. Alloy. Compd.* **2017**, 698, 906–912.

[3] Keast, V.J.; Williams, D.B. Grain boundary chemistry. *Curr. Opin. ST. M.* **2001**, 5, 23–30.

[4] Yang, J.B.; Yang, Z.G.; Nagai, Y.; Hasegawa, M. A crystallographic model of FCC/BCC martensitic nucleation and growth. *Acta Mater.* **2010**, 58, 1599–1606.

[5] Lehockey, E.M.; Limoges, D.; Palumbo, G.; Sklarchuk, J.; Tomantschger, K.; Vincze, A. On improving the corrosion

and growth resistance of positive Pbacid battery grids by grain boundary engineering. *J. Power Sources* **1999**, 78(1), 79–83.

[6]   Ayuela, A.; Jaskolski, W.; Chico, L. Electronic properties of graphene grain boundaries. *New J. Phys.* **2014**, 16, 083018.

[7]   Randle, V. Grain boundary engineering: an overview after 25 years. *Mater. Sci. Technol.* **2010**, 26(3), 253–261.

[8]   Watanabe, T. Grain boundary engineering: historical perspective and future prospects. *J. Mater. Sci.* **2011**, 46(12), 4095–4115.

[9]   Song, L. H.; Yu, X. G. Defect engineering in cast mono-like silicon: A review. *Prog. Photovoltaics* **2021**, 29(3), 294–314.

[10] Kutsukake, K.; Usami, N.; Ohno, Y.; Tokumoto, Y.; Yonenaga, I. Mono-like silicon growth using functional grain boundaries to limit area of multicrystalline grains. *IEEE J. Photovolt.* **2014**, 4, 1.

[11] Rittner, J.; Seidman, D. <110> Symmetric tilt grain-boundary structures in fcc metals with low stacking-fault energies. *Phys. Rev. B* **1996**, 54(10), 6999.

[12] Holm, E.A.; Rohrer, G.S.; Foiles, S.M.; Rollett, A.D.; Miller, H.M.; Olmsted, D.L. Validating computed grain boundary energies in fcc metals using the grain boundary character distribution. *Acta Mater.* **2011**, 59(13), 5250–5256.

[13] Tschopp M.A.; Coleman, S.P.; McDowell, D.L.; Symmetric and asymmetric tilt grain boundary structure and energy in Cu and Al (and transferability to other fcc metals), *Integr. Mater. Manuf. Innov.* **2015**, 4(1), 176–189.

[14] Olmsted, D.L. Foiles, S.M., Holm, E.A. Survey of computed grain boundary properties in face-centered cubic metals: I. Grain boundary energy. *Acta Mater.* **2009**, 57, 3694.

[15] Olmsted, D.L.; Holm, E.A.; Foiles, S.M. Survey of computed grain boundary properties in face-centered cubic metals-II: Grain boundary mobility. *Acta Mater.* **2009**, 57, 3704.

[16] Homer, E.R. High-throughput simulations for insight into grain boundary structure-property relationships and other complex microstructural phenomena. *Comput. Mater. Sci.* **2019**, 161, 244–254.

[17] Bair, J.L.; Homer, ER. Antithermal Mobility in Σ7 and Σ9 Grain Boundaries Caused by Stick-Slip Stagnation of Ordered Atomic Motions about Coincidence Site Lattice Atoms. *Acta Mater.* **2019**, 162, 10–18.

[18] Priedeman, J.L.; Olmsted, D.L.; Homer, E.R. The role of crystallography and the mechanisms associated with migration of incoherent twin grain boundaries. *Acta Mater.* **2017**, 131, 553–563.

[19] Homer, E.R. Investigating the mechanisms of grain boundary migration during recrystallization using molecular dynamics. In: 36th Risø International Symposium on Materials Science. Roskilde: IOP Publishing, **2015**, pp.012006.

[20] Homer, E.R.; Holm, E.A.; Foiles, S.M.; Olmsted, D.L. Trends in Grain Boundary Mobility: Survey of Motion Mechanisms. *JOM* **2014**, 66(1), 114–120.

[21] Huang, Q.S.; Yang, W.; Zhou, H.F. Migration of grain boundary triple junctions in nanocrystalline metals initiated by accumulated dislocations. *Int. J. Plasticity* **2024**, 173, 103872.

[22] Page, D.E.; Varela, K.F.; Johnson, O.K.; Fullwood, D.T.; Homer, E.R. Measuring simulated hydrogen diffusion in symmetric tilt nickel grain boundaries and examining the relevance of the Borisov relationship for individual boundary diffusion. *Acta Mater.* **2021**, 212, 116882.

[23] Wagih, M.; Schuh, C.A. Viewpoint: Can symmetric tilt grain boundaries represent polycrystals? *Scr. Mater.* **2023**, 237, 115716.

[24] Wagih, M.; Schuh, C.A. Learning Grain-Boundary Segregation: From First Principles to Polycrystals. *Phys. Rev. Lett.* **2022**, 129, 046102.

[25] Jiang, H.; Szlufarska, I. Small-angle twist grain boundaries as sinks for point defects. *Sci. Rep.* **2018**, 8, 3736.

[26] Jiang, H.; Wang, X.; Szlufarska, I. The multiple roles of small angle tilt grain boundaries in annihilating radiation damage in SiC. *Sci. Rep.* **2017**, 7, 42358.

[27] Zhu, Q.; Samanta, A.; Li, B.; Rudd, R.E.; Frolov, T. Predicting phase behavior of grain boundaries with evolutionary search and machine learning. *Nat. Commun.* **2018**, 9(1), 467.

[28] Han, J.; Vitek, V.; Srolovitz, D.J. Grain-boundary metastability and its statistical properties. *Acta Mater.* **2016**, 104, 259–273.

[29] Meiners, T.; Frolov, T.; Rudd, R.E.; Dehm, G.; Liebscher, C.H. Observations of grain-boundary phase transformations

in an elemental metal. *Nature* **2020**, 579(7799), 375–378.

[30] Zhang, J.; Wang, C.; Ho, K. Finding the low-energy structures of Si[001] symmetric tilted grain boundaries with a genetic algorithm. *Phys. Rev. B* **2009**, 80, 174102.

[31] Yu, Z.Y.; Cantwell, P.R.; Gao, Q.; Yin, D.; Zhang, Y.Y.; Zhou, N.X.; Rohrer, G.S.; Widom, M.; Luo, J.; Harmer, M.P. Segregation-induced ordered superstructures at general grain boundaries in a nickel-bismuth alloy. *Science* **2017**, 358, 97–101.

[32] Von Alfthan, S.; Haynes, P.D.; Kaski, K.; Sutton, A.P. Are the structures of twist grain boundaries in silicon ordered at 0K. *Phys. Rev. Lett.* **2006**, 96, 055505.

[33] Shiihara, Y.; Kanazawa, R.; Matsunaka, D.; Lobzenko, I.; Tsuru, T.; Kohyama, M.; Mori, H. Artificial neural network molecular mechanics of iron grain boundaries. *Scr. Mater.* **2021**, 207, 114268.

[34] Yokoi, T.; Kato, H.; Oshima, Y.; Matsunaga, K. Atomic structures of grain boundaries for Si and Ge: A simulated annealing method with artificial-neural-network interatomic potentials. *J. Phys. Chem. Solids* **2022**, 173, 111114.

[35] Yokoi, T.; Matsuura, M.; Oshima, Y.; Matsunaga, K. Grain-boundary thermodynamics with artificial-neural-network potential: Its ability to predict the atomic structures, energetics, and lattice vibrational properties for Al. *Phys. Rev. Mater.* **2023**, 7(5), 053803.

[36] Gomberg, J.A.; Medford, A.J.; Kalidindi, S.R. Extracting knowledge from molecular mechanics simulations of grain boundaries using machine learning. *Acta Mater.* **2017**, 133, 100–108.

[37] Rosenbrock, C.W.; Homer, E.R.; Csányi, G.; Hart, G.L.W. Discovering the building blocks of atomic systems using machine learning: application to grain boundaries. *npj Comput. Mater.* **2017**, 3(1), 29.

[38] Sharp, T.A.; Thomas, S.L.; Cubuk, E.D.; Schoenholz, S.S.; Srolovitz, D.J.; Liu, A.J. Machine learning determination of atomic dynamics at grain boundaries. *Proc. Natl. Acad. Sci.* **2018**, 115(43), 10943–10947.

[39] Priedeman, J.L.; Rosenbrock, C.W.; Johnson, O.K.; Homer, E.R. Quantifying and connecting atomic and crystallographic grain boundary structure using local environment representation and dimensionality reduction techniques. *Acta Mater.* **2018**, 161, 431–443.

[40] Homer, E.R.; Hensley, D.M.; Rosenbrock, C.W.; Nguyen, A.H.; Hart, G.L.W. Machine-learning informed representations for grain boundary structures. *Front. Mater.* **2019**, 6, 168.

[41] Patala, S. Understanding grain boundaries - the role of crystallography, structural descriptors and machine learning, *Comput. Mater. Sci.* **2019**, 162, 281–294.

[42] Otsuki, A. Energies of (001) twist grain boundaries in silicon. *Acta Mater.* **2001**, 49, 1737–1745.

[43] Wang, L.; Yu, W.S.; Shen, S.P. Revisiting the structures and energies of silicon <110> symmetric tilt grain boundaries. *J. Mater. Res.* **2019**, 34(6), 1021–1033.

[44] Von Alfthan, S.; Kaski, K.; Sutton, A.P. Order and structural units in simulations of twist grain boundaries in silicon at absolute zero. *Phys. Rev. B* **2006**, 74, 134101.

[45] Baruffi, C.; Brandl, C. On the structure of (111) twist grain boundaries in diamond: atomistic simulations with Tersoff-type interatomic potentials. *Acta Mater.* **2021**, 215, 117055.

[46] Read, W.T.; Shockley, W. Dislocation models of crystal grain boundaries. *Phys. Rev.* **1950**, 78(3), 275–289.

[47] Frank, F.C. Conference on plastic deformation of crystalline solids. Carnegie Institute of Technology and Office of Naval Research. **1950**, 150.

[48] Bilby, B.A. Continuous distribution of dislocations. *Prog. Solid. Mech.* **1960**, 1, 329.

[49] Yang, J.B.; Nagai, Y.; Hasegawa, M. Use of the Frank–Bilby equation for calculating misfit dislocation arrays in interfaces. *Scr. Mater.* **2010**, 62(7), 458–461.

[50] Yang, J.B.; Nagai, Y.; Yang, Z.G.; Hasegawa, M. Quantization of the Frank–Bilby equation for misfit dislocation arrays in interfaces. *Acta Mater.* **2009**, 57, 4874–4881.

[51] Sangghaleh, A.; Demkowicz, M.J. AIDA: a tool for exhaustive enumeration of solutions to the quantized Frank-Bilby equation. *Comput. Mater. Sci.* **2018**, 145, 35–47.

[52] Sutton, A.P. On the structural unit model of grain boundary structure. *Philos. Mag. Lett.* **1989**, 59(2), 53–59.

[53] Han, J.; Vitek, V.; Srolovitz, D.J. The grain-boundary structural unit model redux. *Acta Mater.* **2017**, 133, 186–199.

[54] Banadaki, A.D.; Patala, S. A three-dimensional polyhedral unit model for grain boundary structure in fcc metals. *npj Comput. Mater.* **2017**, 3(1), 13.

[55] Winter, I.S.; Rudd, R.E; Oppelstrup, T.; Frolov, T. Nucleation of Grain Boundary Phases. *Phys. Rev. Lett.* **2022**, 128, 035701.

[56] Winter, I.S.; Oppelstrup, T.; Frolov, T.; Rudd, R.E. Characterization and visualization of grain boundary disconnections. *Acta Mater.* **2022**, 237, 118067.

[57] Saylor, D.M.; Morawiec, A.; Rohrer, G.S. The relative free energies of grain boundaries in magnesia as a function of five macroscopic parameters. *Acta Mater.* **2003**, 51(13), 3675–3686.

[58] Brink, T.; Langenohl, L.; Bishara, H.; Dehm, G. Universality of grain boundary phases in fcc metals: Case study on high-angle [111] symmetric tilt grain boundaries. *Phys. Rev. B* **2023**, 107(5), 054103.

[59] Homer, E.R.; Patala, S.; Priedeman, J.L. Grain boundary plane orientation fundamental zones and structure-property relationships. *Sci. Rep.* **2015**, 5, 15476.

[60] Erickson, H.C.; Homer, E.R. Insights into grain boundary energy structure-property relationships by examining computed [1 0 0] disorientation axis grain boundaries in Nickel. *Scr. Mater.* **2020**, 185, 165–169.

[61] Patala, S.; Schuh, C.A. Symmetries in the representation of grain boundary plane distributions. *Philos. Mag.* **2013**, 93(5). 524–573.

[62] Baird, S.G.; Homer, E.R.; Fullwood, D.T.; Johnson, O.K. Five degree-of-freedom property interpolation of arbitrary grain boundaries via Voronoi fundamental zone framework. *Comput. Mater. Sci.* **2021**, 200, 110756.

[63] Homer, E.R.; Hart, G.L.W.; Owens, C.B.; Hensley, D.M.; Spendlove, J.C.; Serafinb, L.H. Examination of computed aluminium grain boundary structures and energies that span the 5D space of crystallographic character. *Acta Mater.* **2022**, 234, 118006.

[64] Morawiec, A.; Glowinski, K. On "macroscopic" characterization of mixed grain boundaries. *Acta Mater.* **2013**, 61, 5756–5767.

[65] Morawiec, A. On the frequency of occurrence of tilt and twist grain boundaries. *Scr. Mater.* **2009**, 61(4), 438–440.

[66] Wan, W.; Tang, C.X. Structures and energies of computed silicon (001) small angle mixed grain boundaries as a function of three macroscopic characters. *Acta Mater.* **2023**, 261, 119353.

[67] Yang, J.B.; Nagai, Y.; Hasegawa M.; Osetsky, Y.N. Atomic scale modeling of {110} twist grain boundaries in a-iron: structure and energy properties. *Philos. Mag.* **2010**, 90, 991–1000.

[68] Yang, J.B.; Osetsky, Y.N.; Stoller, R.E.; Nagai, Y.; Hasegawa, M. The effect of twist angle on anisotropic mobility of {110} hexagonal dislocation networks in alpha-iron. *Scr. Mater.* **2012**, 66, 761–764.

[69] Wan, W.; Tang, C.X.; Zou, W.N. Exploring Silicon [001] Small Angle Symmetric Tilt Grain Boundaries: Structures, Energies and Stress fields. *Appl. Surf. Sci.* **2022**, 599, 153828.

[70] Tang, C.X.; Wan, W.; Huang, L.F.; He, R.C.; Zhou, L. On the Formation and Multiplicity of Si [001] Small Angle Symmetric Tilt Grain Boundaries: Atomistic Simulation of Directional Growth. *Cryst. Growth Des.* **2022**, 22, 7491–7500.

[71] Wan, W.; Sun, Z.P.; Xiong, Z.K. Tang, C.X. Misorientation and Temperature Dependence of Small Angle Twist Grain Boundaries in Silicon: Atomistic Simulation of Directional Growth. *Cryst. Growth Des.* **2023**, 23, 2893–2904.

[72] Neily, S.; Youssef, S.; Fournel, F.; Bonnet, R. The angular dislocation parallel to a free surface: Application to a (111)Si low-angle twist boundary. *Philos. Mag.* **2011**, 91(31), 4001–4012.

[73] Fournel, F.; Moriceau, H.; Aspar, B. Accurate control of the misorientation angles in direct wafer bonding. *Appl. Phys. Lett.* **2002**, 80, 793.

[74] Akatsu, T.; Scholz, R.; Gosele, U. Dislocation structure in low-angle interfaces between bonded Si(001) wafers. *J. Mater. Sci.* **2004**, 39(9), 3031–3039.

[75] Vdovin, V.I.; Ubyivovk, E.V.; Vyvenko, O.F. Regularities in the Formation of Dislocation Networks on the Boundary of Bonded Si (001) Wafers. *Semiconductors* **2013**, 47(2), 264–268.

[76] Vdovin, V.I.; Vyvenko, O.F.; Ubyivovk, E.V.; Kononchuk, O. Mechanisms of Dislocation Network Formation in Si(001) Hydrophilic Bonded Wafers. *Solid State Phenomena* **2011**, 178, 253.

[77] Wilhelm, T.; Kuhlmann, V.; Scheerschmidt, K. Bonded semiconductor interfaces with twist and tilt rotation: TEM analysis supported by molecular dynamics structure modelling. *Phys. Stat. Sol. C* **2007**, 4(8), 3115–3119.

[78] Lim, A.T.; Haataja, M.; Cai, W.; Srolovitz, D.J. Stress-driven migration of simple low-angle mixed grain boundaries. *Acta Mater.* **2012**, 60, 1395–1407.

[79] Thompson, A.P.; Aktulga, H.M.; Berger, R.; Bolintineanu, D.S.; Brown, W.N.; Crozier, P.S.; Veld, P.J.I.; Kohlmeyer, A.; Moore, S.G.; Nguyen, T.D.; Shan, R.; Stevens, M.J.; Tranchida, J.; Trott, C.; Plimpton, S.J. LAMMPS-a flexible simulation tool for particle-based materials modeling at the atomic, meso, and continuum scales. *Comput. Phys. Commun.* **2021,** 271, 108171.

[80] Kumagai, T.; Izumi, S.; Hara, S.; Sakai, S. Development of bond-order potentials that can reproduce the elastic constants and melting point of silicon for classical molecular dynamics simulation. *Comput. Mater. Sci.* **2007**, 39(2), 457–464.

[81] Kresse, G.; Furthmüller, J. Efficiency of ab-initio total energy calculations for metals and semiconductors using a plane-wave basis set. *Comput. Mater. Sci.* **1996**, 6, 15–50.

[82] Kresse, G.; Furthmüller, J. Efficient iterative schemes for ab initio total-energy calculations using a plane-wave basis set. *Phys. Rev. B* **1996**, 54, 11169.

[83] Perdew, J.P.; Burke, K.; Ernzerhof, M. Generalized gradient approximation made simple. *Phys. Rev. Lett.* 1996, 77, 3865–3868.

[84] Blöchl, P. E. Projector augmented-wave method. *Phys. Rev. B* **1994**, 50, 17953.

[85] Stukowski, A.; Bulatov, V. V.; Arsenlis, A. Automated identification and indexing of dislocations in crystal interfaces. *Model. Simul. Mater. Sc.* **2012**, 20, 85007.

[86] Stukowski, A. Visualization and analysis of atomistic simulation data with ovito–the open visualization tool. *Model. Simul. Mater. Sc.* **2010**, 18, 015012.

[87] Wan, W.; Tang, C.X.; Zhang, J.J.; Zhou, L. General molecular dynamics approach to understand the mechanical anisotropy of monocrystalline silicon under the nanoscale effects of point defect. *Nanomaterials* **2021**, 11(8), 1965.

[88] Bulatov, V.V.; Reed, B.W.; Kumar, M. Grain boundary energy function for fcc metals. *Acta Mater.* **2014**, 65, 161–175.

[89] Chirayutthanasak, O.; Sarochawikasit, R.; Khongpia, S.; Okita, T.; Dangtip, S.; Rohrer, G.S.; Ratanaphan, S. Universal function for grain boundary energies in bcc metals. *Scr. Mater.* **2024**, 240, 115821.

[90] Ke T.S. A Grain Boundary Model and the Mechanism of Viscous Intercrystalline Slip. *J. Appl. Phys.* **1949**, 20(3), 274-280.

[91] Reiche, M.; Kittler, M.; Scholz, R.; Hähnel, A.; Arguirov, T. Structure and properties of dislocations in interfaces of bonded silicon wafers. *Journal of Physics: Conference Series* **2011**, 281, 012017.

[92] Bonnet, R.; Couillard, M.; Dhouibi, S.; Neily, S. Atomic scale displacement field induced by a near-Σ9 twin boundary in silicon. *Phys. Status Solidi B*, **2016**, 1–4.

[93] Dai, S.Y.; Xiang, Y.; Srolovitz, D.J. Structure and energy of (1 1 1) low-angle twist boundaries in Al, Cu and Ni. *Acta Mater.* **2013**, 61, 1327–1337.

[94] Dai, S.Y.; Xiang, Y.; Srolovitz, D.J. Atomistic, generalized peierls-nabarro and analytical models for (111) twist boundaries in al, cu and ni for all twist angles. *Acta Mater.* **2014**, 69, 162–174.

[95] Wolf, D. A Read-Shockley model for high-angle grain boundaries, *Scr. Metall.* **1989**, 23(10), 1713–1718.

[96] Schwartz, D.; Bristowe, P.D.; Vitek, V. Dislocation structure and energy of high angle [001] twist boundaries: A computer simulation study. *Acta Metall.* **1988**, 36(3), 675–687.

[97] Holm, E.A.; Olmsted, D.L.; Foiles, S.M. Comparing grain boundary energies in face-centered cubic metals: Al, Au, Cu and Ni *Scr. Mater.* **2010**, 63, 905-908.